ELSEVIER

Contents lists available at ScienceDirect

Theoretical and Applied Mechanics Letters

journal homepage: www.elsevier.com/locate/taml



On the impact of debris accumulation on power production of marine hydrokinetic turbines: Insights gained via LES



Mustafa Meriç Aksen, Kevin Flora, Hossein Seyedzadeh, Mehrshad Gholami Anjiraki, Ali Khosronejad*

Department of Civil Engineering, Stony Brook University, Stony Brook, NY 11794, USA

ARTICLE INFO

Keywords:
Large-eddy simulations
Marine hydrokinetic turbine
Actuator models
Debris accumulations
Debris model

ABSTRACT

We present a series of large-eddy simulations to systematically investigate the impact of debris accumulation on the hydrodynamics and power production of a utility-scale marine hydrokinetic (MHK) turbine under various debris loads lodged on the upstream face of the turbine tower. The turbine blades are modeled using turbine resolving, actuator line, and actuator surface methods. Moreover, the influence of debris on the flow field is captured by directly resolving individual logs and employing a novel debris model. Analyzing the hydrodynamics effects of various debris accumulations, we show that an increase in the density of debris accumulation leads to more flow bypassing beneath the turbine blade. This, in turn, reduces the flow momentum that reaches the MHK blades at the lower depths, inducing significant fluctuation in power production. Further, it is shown that debris-induced turbulent fluctuations contribute to significant variability in the MHK turbine's power production.

1. Introduction. Marine hydrokinetic turbine (MHK) devices offer the advantage of harnessing clean energy from tides, rivers, and streams [1]. As they become more widespread in aquatic environments, such devices will increasingly assume a more meaningful role in enhancing renewable energy generation [2]. Hence, it is essential to investigate the sustainability of MHK turbines in their interactions with the natural environment. In particular, installing MHK turbines in the dynamic nature of evolving fluvial environments with natural vegetation may lead to unpredictable issues, such as the accumulation of floating wood debris [3-6]. As channel planforms evolve through lateral migration in natural waterways, forces in riverine flows erode channel banks, causing bankline trees to fall into the flow and become driftwood [7]. Such floating debris is often transported as individual logs and moves along the thalweg of the stream [8-10] and can eventually accumulate on manufactured structures. Such debris accumulation could impose detrimental consequences such as backwater rise, excessive structural loading, and extensive scour around the structures [3,4,7]. The positioning of individual woody logs over the man-made structures in waterways is random. As a result, the significant features of debris accumulation (e.g., compactness, accumulation length, and permeability) could vary randomly, contributing to the complicated nature of turbulent flow around such natural buildups [11]. Jeon et al. [12] studied the accumulation of floating debris on the laboratory-scale models of bridge foundations. Their study revealed the significant impact of woody debris on the flow field and sediment transport past the bridge foundations.

Past studies have investigated the impact of debris accumulation and sedimentation on bridge piers [10]. Furthermore, laboratory investigations revealed that while static turbine components induce typical bridge pier scour mechanisms, introducing rotating turbine components intensifies local shear stress, enhancing and advancing the scour behaviors [13]. Recent laboratory studies have extended their scope by considering coupled turbine performance [14] and meandering channels [15]. Later, Musa et al. [16] studied the impact of mobile bed sand waves on the performance and stability of MHK turbine arrays. Yang et al. [17] developed a computational model for bed-load sediment transport under clear-water conditions. Such studies have added a great deal to our current understanding of sediment dynamics impacts on the performance of MHK turbines (also see, e.g., [18-21]). However, the impact of debris accumulation on the performance of MHK turbines has not been addressed in previous studies. The lack of such studies could be attributed to the complexity of the interaction between debris and MHK turbines in natural settings. However, experimental studies may not be practical due to limitations in Reynolds number [22-26] and challenges in creating scaled models of realistic debris shapes. To address this knowledge gap, we carried out a systematic investigation using our in-house high-fidelity numerical modeling tool to gain insight into the intricate interaction of debris and a single utility-scale MHK turbine and better understand the impact of debris on the power production of the MHK

The present numerical study of debris impact on a utility-scale MHK turbine involves the following procedures for modeling various aspects

E-mail address: ali.khosronejad@stonybrook.edu (A. Khosronejad).

^{*} Corresponding author.

of the fluid-structure interaction problem: (1) large-eddy simulation (LES) is employed to resolve the flow field while the near-solid surfaces are resolved using a wall-modeling approach; (2) a turbine-resolving approach (based on the immersed boundary method) and various actuator model techniques are utilized to numerically capture the MHK turbine's blades, nacelle and tower; and (3) a geometry-resolving method and a novel debris-model technique is used to capture the effect of accumulated debris on the flow. The recent advancements in high-performance computing (HPC), wall-modeling techniques, and the immersed boundary method have enabled us to carry out the LES of the utility-scale MHK turbine [24,27]. In particular, the model reduced the need for a high-resolution grid system around turbine blades, tree logs, and other solid surfaces [24]. At the same time, the use of an HPC cluster allowed for the LES of the test case to capture a wide range of turbulent eddies and resolve the instantaneous flow filed past the debris and MHK turbines.

The MHK turbines are generally resolved using four increasingly sophisticated approaches: (1) turbine-resolving (TR), (2) actuator disk parameterization (AD), (3) actuator line parameterization (AL), and (4) actuator surface parameterization (AS). The TR approach requires a significant number of grid nodes to represent the boundary layer around the turbine accurately [28,29]. The TR approach serves as reference solutions for reduced-order approaches as it can capture the physics of turbine and flow interactions [30-32]. Yet, given the TR method's intricate and highly detailed nature, it may not be practical for simulating utility-scale tidal farms [25,28]. For that, actuator models play a pivotal role in reducing the computational costs while maintaining reasonable computational accuracy of tidal farm modeling studies. The AL and AS models provide a higher level of accuracy by accounting for the impact of rotational effects, finite blade numbers, and nonuniform force distribution in the azimuthal direction [33]. As detailed in [34], the AL concept represents the turbine blade as a rotating line. The line experiences distributed forces computed through a blade element method combined with predetermined 2D airfoil drag and lift coefficients (e.g., [35-38]). Kang et al. [25] utilized high-resolution LES of the TR method. They compared its results with those obtained from the AL and AD models, showing that both actuator models predicted significantly smaller-scale wake meandering compared to the findings of the TR model and the experimental data. Yang et al. [28] conducted the LES of the AL model to simulate a wind farm suited to a complex terrain. Ouro et al. [39] and Ouro et al. [40] employed the AL parametrization approach to calculate the power generation of MHK turbines [41,42].

On the other hand, the AS can be employed as an alternative to the AL and AD models due to certain limitations of these models. These limitations include the absence of an effective nacelle model and the inability to capture more intricate geometrical aspects of the turbine blade by refining the mesh [33]. In the AS model, the blade element method calculates the forces. These forces are distributed across the surface created by the chord lines of the foils at various radial positions [33,43,44]. For instance, Li and Yang [43] employed the AS method in combination with the curvilinear immersed boundary (CURVIB) method to simulate the flow around a propeller. Certain studies also incorporate an AS model for the nacelle to enhance the realism of simulations. This approach determines normal forces by adhering to non-penetration boundary conditions, similar to the direct forcing immersed boundary method. Meanwhile, the calculation of tangential forces relies on a friction coefficient and a reference velocity of the incoming flow [33,43,44].

Finally, the effect of woody debris on the hydrodynamics is calculated by (1) directly resolving the geometry of individual logs and (2) implementing a debris model to represent their hydrodynamics effect [45]. Needless to say, the geometry-resolving method could accurately represent the hydrodynamics effect of woody pieces on the turbulent flow and power production of MHK turbines at a relatively higher computational cost, especially when abundant debris-like structures are present. Therefore, mid-fidelity surface roughness methods, such as debris models, have been extensively applied on various flows (e.g., see [46–51]).

Herein, we carry out a systematic analysis to demonstrate the effect of randomly distributed debris on the hydrodynamics and power production of a horizontal-axis utility-scale MHK turbine using LES. More specifically, we compare the flow and power generation of a baseline MHK case without any debris to six cases with increasing debris density. Examining the power production of various cases using various turbine resolving methods, we attempt to estimate the loss of power production and reduction in power efficiency due to multiple densities of debris accumulations. Additionally, we investigate the efficiency and accuracy of a mid-fidelity model of debris accumulation through numerical experiments. Such models can later facilitate extending debris-flow-MHK turbine interactions to advanced studies of MHK turbine arrays with complex natural terrains.

This paper is structured as follows. Section 2 outlines the governing equations, flow boundary conditions, and models used for turbine parametrization. Section 3 describes the test case and the computational details. Section 4 presents the simulation results and discussions. Finally, in Section 5, we summarized the findings of the study.

2. Governing equation.

2.1 Hydrodynamics. We solve the spatially filtered Navier-Stokes equations governing incompressible flows in non-orthogonal generalized curvilinear coordinates. Using the compact Newton notation, where repeated indices imply summation, the equations read as follows (i, j, k, l = 1, 2, 3) [52]:

$$J\frac{\partial U^j}{\partial \xi^j} = 0,\tag{1}$$

$$\frac{\partial U^{i}}{\partial t} = \frac{\xi_{i}^{i}}{J} \left[\frac{\partial}{\partial \xi^{j}} \left(U^{j} u_{i} \right) + \frac{1}{\rho} \frac{\partial}{\partial \xi^{j}} \left(\mu \frac{g^{jk}}{J} \frac{\partial u_{i}}{\partial \xi^{k}} \right) - \frac{1}{\rho} \frac{\partial}{\partial \xi^{j}} \left(\frac{\xi_{i}^{j} P}{J} \right) \right. \\
\left. - \frac{1}{\rho} \frac{\partial \tau_{ij}}{\partial \xi^{j}} + F_{\text{AM},l} + F_{\text{DM},l} \right], \tag{2}$$

where J denotes the Jacobian of the geometric transformation, $J=\left|\frac{\partial(\xi^1,\xi^2,\xi^3)}{\partial(x_1,x_2,x_3)}\right|$; $\xi^i_j=\frac{\partial\xi^i}{\partial x_j}$ represents the transformation metric; u_i stands for the filtered ith Cartesian velocity component; U^i is the filtered contravariant volume flux, computed as $U^i=(\frac{\xi^i_m}{J})u_m$, where ξ^i_m is a component of the transformation metric; $g^{jk}=\xi^k_l\xi^k_l$ represents the components of the contravariant metric tensor; P is the filtered pressure; ρ is the fluid's density; μ is the fluid's dynamic viscosity; and τ_{ij} is the subgrid stress (SGS) tensor used in the LES turbulence model. The SGS terms are modeled using the Smagorinsky model [52]:

$$\tau_{ij} - \frac{1}{3} \tau_{kk} \delta_{ij} = -2\mu_t \overline{S_{ij}},\tag{3}$$

where the grid filtering operation is indicated by the overbar notation; S_{ij} is the strain rate tensor after filtering; μ_t is the eddy viscosity that is expressed as

$$\mu_{\rm t} = \rho C_{\rm s} \Delta^2 |\overline{S}|,\tag{4}$$

where $C_{\rm s}$ is the Smagorinsky constant and determined using the dynamic Smagorinsky model that is implemented within the framework of the CURVIB method [53]; and Δ refers to the filter width dictated by grid resolution. The actuator and debris models are included in the flow solver, with the source terms introduced as $F_{{\rm AM},l}$ and $F_{{\rm DM},l}$ in Eq. (2), respectively.

2.2 Curvilinear immersed boundary. The CURVIB method adeptly manages complex geometries with constant or dynamic boundaries interacting with fluids [54]. The solid surfaces of bodies, i.e., the channel geometry, turbine blades, nacelle, tower, and woody debris are discretized using unstructured triangular grid systems and immersed into the structured background grid system of the flow domain. The immersed bodies within the computational domain are treated as a sharp interface [55]. At the beginning of each time step, the CURVIB approach recalculates boundary conditions at nearby background grid nodes using the local normal direction interpolation [53]. These grid points are arranged

based on their proximity to the immersed body (i.e., turbine, blades, channel, and debris). The background grid nodes are categorized into three groups, including fluid nodes, on which the governing equations of the flow field are solved; solid nodes that are located inside the solid surfaces of the immersed bodies and excluded from computations; and immersed boundary nodes (i.e., IB nodes) which are the nodes adjacent to the surfaces of immersed bodies within the fluid domain [56]. Although the advantage of the CURVIB method is recognizing movable boundaries, reclassification is done at the beginning of every time step, rendering this process computationally expensive. We employ the raytracing algorithm introduced by Borazjani et al. [57] to minimize the computational cost of reclassification. In this approach, the immobile bodies (i.e., turbine tower, debris, channel) are classified only once at the beginning of the computations, while this procedure should be repeated in each time step to reclassify the mobile bodies, such as turbine blades and nacelle [53]. The velocity field is reconstructed at the IB nodes, and to avoid the need to resolve the flow near the solid surfaces with a very fine grid system, a wall model is implemented [52,58,59].

2.3 Wall model. The wall model employed in this work relies on simplified equations describing a thin boundary layer, expressed as follows:

$$\frac{1}{\rho} \frac{\partial}{\partial l} \left[\left(\mu + \mu_t' \right) \frac{\partial u_s}{\partial l} \right] = 0, \tag{5}$$

where μ_1' represents the near-wall eddy viscosity, u_s is the velocity parallel to the immersed boundary surface, and l and s correspond to the normal and tangential directions. The eddy viscosity is determined through the mixing length model with near-wall damping, outlined as follows:

$$\mu'_{t}(l) = \mu \kappa l^{+} (1 - e^{-l^{+}/19})^{2},$$
(6)

where l^+ represents the dimensionless mixing length defined as $\rho u_\tau l/\mu$, with u_τ denoting the near-wall shear velocity, and κ is the con Kármán constant (=0.4). The tangential velocity component u_s , at every IB node is obtained from the integration of Eq. (5) in the direction normal to the wall [53]:

$$u_{s}(\delta_{B}) = \frac{\int_{0}^{\delta_{B}} \frac{1}{\mu + \mu_{t}} dI}{\int_{0}^{\delta_{C}} \frac{1}{\mu + \mu_{t}} dI} \left[u_{s}(\delta_{C}) - u_{s}(0) \right] + u_{s}(0), \tag{7}$$

where δ_B is the distance of the closest IB node from the wall; δ_C is the distance of the interception point of two adjacent fluid nodes closest to the IB node from the wall; and $u_s(0)$ and $u_s(\delta_C)$ correspond to the tangential velocity component at the solid surface and δ_C away from the solid surface, respectively.

2.4 Debris model. We implemented a debris model that represents the effect of debris on the hydrodynamics at a lower computational cost than the debris-resolving approach. In this model, the volume of the flow occupied by the debris is discretized using an unstructured triangular grid system. The fluid nodes inside this volume are identified, and a drag force (denoted as $F_{\mathrm{DM},j}$ in Eq. (2)) is applied to the equations of motion at those nodes. The drag force is obtained as follows [48]:

$$F_{\text{DM},i} = -\rho C_{\text{d}} A_{\text{f}} (u_i u_i)^{1/2} u_i \delta(x_k - X_k) s, \tag{8}$$

where $C_{\rm d}$ is the drag coefficient of the debris and is set equal to 1.2; $A_{\rm f}$ is the projected area of the debris accumulation per unit volume, i.e., the frontal area density; and δ is the Dirac delta, which is a function to determine whether a grid node x_k is located inside the debris volume or on the outside of the debris volume X_k . For the sake of simplicity, we employed a constant $C_{\rm d}$ for the debris model. This is consistent with the past studies in which the riverine vegetation was modeled using a constant drag coefficient for the vegetation model [45,49,54,59]. Additionally, the frontal area, which could be expressed using a vertical profile, varies as a function of the tree type. For the sake of simplicity, however, we assume that the debris model has a uniformly distributed frontal area vertically (for more details, see [49,60–62]).

2.5 Actuator models.

 $2.5.1\,AS$ model. Actuator models offer a simplified mathematical representation of marine turbine rotor blades. In the AS model, the surface forces on the blade and nacelle of a marine turbine rotor are incorporated into the equations of motion [33]. As such, the lift and drag forces of the blade and nacelle are computed over the Lagrangian grid nodes (i.e., the unstructured triangular grid system that discretizes the surfaces of the blade and nacelle) of the actuator surfaces. The Lagrangian grid system of the actuator surface, denoted as x, y, and z are immersed into the background structured grid system of the fluid nodes, denoted as X, Y, and Z. The blade and nacelle geometries are prescribed as surfaces constructed by the chord lines situated at various radial positions along the blade and nacelle. The drag and lift forces are then computed as follows [63]:

$$\mathbf{F}_{L} = \frac{1}{2}c\rho C_{L} |\mathbf{V}_{rel}|^{2} \mathbf{e}_{L},\tag{9}$$

$$\mathbf{F}_{\mathrm{D}} = \frac{1}{2} c \rho C_{\mathrm{D}} |\mathbf{V}_{\mathrm{rel}}|^2 \mathbf{e}_{\mathrm{D}},\tag{10}$$

where $C_{\rm D}$ and $C_{\rm L}$ are the tabulated drag and lift coefficients; c is the chord length; $e_{\rm L}$ and $e_{\rm D}$ are the unit vectors in the directions of lift and drag; and $V_{\rm rel}$ is the relative incoming velocity at each radial location, expressed as [63]:

$$\mathbf{V}_{\text{rel}} = \left(u_x, u_\theta - \Omega r\right),\tag{11}$$

where u_x and u_θ represent the averaged flow velocities at different radial points along the chord length of the blade, in axial and azimuthal directions, respectively. These values are calculated using the equation provided as follows:

$$u_{x} = \frac{1}{c} \int_{c} \mathbf{u}(\mathbf{X}) \cdot \mathbf{e}_{x} ds, \tag{12}$$

$$u_{\theta} = \frac{1}{c} \int_{c} \mathbf{u}(\mathbf{X}) \cdot \mathbf{e}_{\theta} ds, \tag{13}$$

where Ω is the rotational speed of the turbine rotor, and r is the distance from the rotor center to the blade element. Using the discrete delta function δ_h , the velocity vector from the fluid nodes is transferred to the line elements and, thus, the reference velocity at the line elements is calculated as follows [64]:

$$\mathbf{u}(\boldsymbol{X}) = \sum_{G_X} \mathbf{u}(\boldsymbol{x}) \delta_h(\boldsymbol{x} - \boldsymbol{X}) V(\boldsymbol{x}), \tag{14}$$

where G_x comprises the cells in the background grid and V(x) is the volume of the fluid cells defined as

$$V = h_{x}h_{y}h_{\tau},\tag{15}$$

where h_x , h_y , and h_z are the grid spacing in the Cartesian coordinates, i.e., x, y, and z directions, and the discrete delta function is expressed as:

$$\delta_h(\mathbf{x} - \mathbf{X}) = \frac{1}{V} \phi \left(\frac{\mathbf{x} - \mathbf{X}}{h_{\mathbf{x}}} \right) \phi \left(\frac{\mathbf{y} - \mathbf{Y}}{h_{\mathbf{y}}} \right) \phi \left(\frac{\mathbf{z} - \mathbf{Z}}{h_{\mathbf{z}}} \right), \tag{16}$$

where ϕ is the smoothed four-point cosine function, and the lift and drag coefficients are the parameters affected by the Reynolds number and the angle of attack. The angle of attack is computed as

$$\alpha = \phi - \gamma,\tag{17}$$

$$\phi = -\arctan\left[u_x/\left(u_\theta - \Omega r\right)\right],\tag{18}$$

where γ represents the angle that encompasses the blade pitch. To adjust the 2D lift and drag coefficients to account for the tip loss effect, a corrective function, denoted as F_1 is applied [65]. This correction is

essential for addressing the rotational impacts and those induced by the finite aspect ratio of the blade. F_1 function is described as:

$$F_1 = \frac{2}{\pi} a \cos \left\{ \exp \left[-g \frac{B(R-r)}{2r \sin \phi} \right] \right\},\tag{19}$$

$$g = \exp\left[-0.125(B\lambda - 21)\right] + 0.1,\tag{20}$$

where B is the number of blades, R is the rotor radius, and λ is the tip speed ratio [65]. Assuming a uniform distribution over chordwise direction, for each radial point along the blades, we calculate the force per unit area acting on the actuator as follows:

$$f(X) = (\mathbf{F}_{L} + \mathbf{F}_{D})/c. \tag{21}$$

The forces acting on the background fluid nodes are computed as follows:

$$f_{AS}(\mathbf{x}) = -\sum_{D_Y} f(\mathbf{X}) \delta_h(\mathbf{x} - \mathbf{X}) A(\mathbf{X}), \tag{22}$$

where the area of the actuator surface grid cells is represented as A(X) and D_X comprises the cells on the actuator surface grid.

As noted above, the parametrization of nacelle geometry can be achieved using the AS approach. This involves considering a distributed friction force across the nacelle surface, comprising tangential and normal force components on the actuator surface. The normal force component per unit area arises from the impermeability of the nacelle, as follows [33]:

$$f_n = \frac{h\widetilde{u_n}}{\Delta t},\tag{23}$$

where $h = (\Delta x \Delta y \Delta z)^{\frac{1}{3}}$ is the length scale of the Eulerian grid, and $\widetilde{u_n}$ denotes the velocity normal to the actuator surface of the nacelle. The expression for the tangential force component is expressed as:

$$f_{\tau} = \frac{1}{2} \rho C_{\rm f} U^2,\tag{24}$$

where $C_{\rm f}$ represents the friction coefficient, which is determined through the following empirical relation [33]:

$$C_{\rm f} = 0.37 (\lg Re_x) - 2.584, \tag{25}$$

where Re_x denotes the local Reynolds number, calculated based on the incoming velocity and the distance from the leading edge of the nacelle. Once the individual forces are obtained, they are projected onto the Eulerian grid using a smoothed cosine discrete delta function, akin to the approach used in the AS model for the blade. The obtained AS forces, $f_{\rm AS}$, are then incorporated into the equations of motion (Eq. (2)), as the external forces per unit volume ($F_{\rm AM}I$).

2.5.2 AL model. The AL model calculates the effect of blades on the flow by assigning forces along each line, representing the blades as linear and rotating structures. Furthermore, the forces on each segment are computed considering variables such as the incoming reference velocity and the specific drag and lift coefficients pertaining to the 2D hydrofoil. Each blade is partitioned into radial segments, and subsequently, the forces acting on each segment of the blades [28] are obtained, and the distributed forces are determined. Once the lift and drag forces at each line element are computed with Eqs. (9) and (10), respectively, the distributed body force over the fluid nodes is obtained as follows:

$$f_{\rm AL}(\mathbf{x}) = \sum_{N_{\rm I}} f(\mathbf{X}) \delta_h(\mathbf{x} - \mathbf{X}) A(\mathbf{X}), \tag{26}$$

where $N_{\rm L}$ is the number of segments of the actuator lines representing the blades, f(X) is the projection of drag and lift forces into the actuator line local coordinates, and A(X) is the length of the discretized actuator line segment [66]. Consequently, the calculated AL force $(f_{\rm AL})$, is used in the equation of motion (Eq. (2)), as the external forces per unit

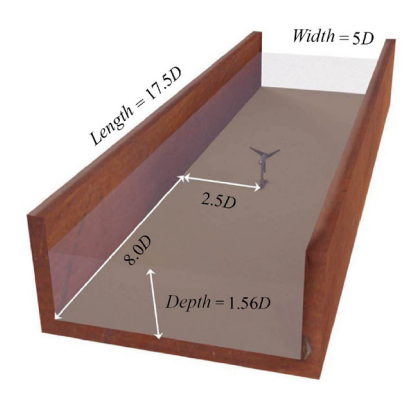


Fig. 1. Schematic of the MHK turbine in the flume. Dimensions are normalized with the rotor diameter D (= 5 m). The turbine's hub height is 0.8D and is located 8D downstream of the inlet. The blockage ratio of the turbine in this flume is 0.10%

volume $(F_{\rm AM,I})$. Finally, the numerical model's hydrodynamics computations are validated against the experimental data of Lee et al. [67] in Section Appendix A.

3. Test case description and computational details. We carried out LES of a horizontal-axis MHK turbine with a rotor diameter of D=5 m. The turbine was placed in a 5D wide, 17.5D long, and 1.56D deep flume (see Fig. 1). The turbine has a hub height of 0.8D that was placed 8D downstream of the channel inlet. The considered turbine is the Gen4 kinetic hydropower system, developed by Verdant Power Inc. The blade profile sections are from the NACA 44 series over the entire blade length, which specifies parameters such as chord, leading edge, camber, mean camber, and thickness, expressed as a proportion of the chord length. Furthermore, a constant tip speed ratio of $\lambda=2.5$ and a bulk flow velocity of $U_{\infty}=1.56$ m/s were considered for all cases. The lift and drag forces at each location along the turbine blades are determined using the lift and drag coefficients of hydrofoils tabulated for a range of angles of attack.

We numerically studied the interaction of flow, turbine, and the debris for four different configurations, including (1) turbine and debris resolving method (TR-DR) (see Fig. 2(a)), (2) AL and debris resolving models (AL-DR) (see Fig. 2(b)), (3) AL and debris models (AL-DM) (see Fig. 2(c)), and (4) AS and debris resolving models (AS-DR) (see Fig. 2(d)).

Moreover, to replicate real-world conditions, virtual debris with various sizes and geometry, which closely imitated naturally fallen wood, were piled randomly over the upstream face of the turbine tower, creating six virtual debris configurations (see Fig. 3). A configuration without a debris pile was considered the baseline case (i.e., case 0). The number of logs in the debris piles, relative porosity, and the frontal area (i.e., the surface area perpendicular to the streamwise direction) of each case are outlined in Table 1. The relative porosity is defined as $1-V_{\rm dr}/V_{\rm dm}$ where $V_{\rm dr}$ is the volume of woody logs and $V_{\rm dm}$ denotes the assumed volume of the debris model. By successive addition of wood branches, we created cases 1 to 6.

Based on a grid sensitivity analysis, reported in Section Appendix B, the computational domain of the flume was discretized using approximately 19 million computational grid nodes with a non-dimensional uniform resolution of 0.02 (normalized with the rotor diameter of 5 m) in all directions. The non-dimensional time step of the computations was

Table 1Parameters of the six debris cases considered in this study. *p* is the percentage of the debris model's volume occupied by the woody logs.

Case	0	1	2	3	4	5	6
Number of logs in pile	0	2	3	5	8	10	12
p (%)	0	97.6	97.2	96.8	95.6	95.0	94.3
Frontal area (m ²)	0	0.473	0.565	0.672	0.886	1.027	1.156

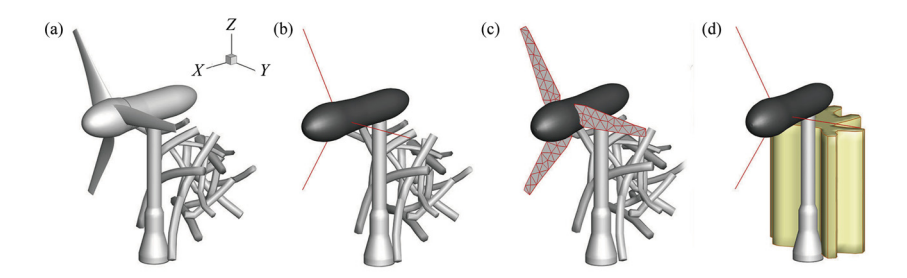


Fig. 2. Numerical experiments are performed for various cases of (a) turbine and debris resolving method (TR-DR); (b) AL and debris resolving models (AL-DR); (c) AL and debris models (AL-DM); and (d) AS and debris resolving models (AS-DR). The lightgray surfaces refer to the parts modeled using the geometry-resolving method, while the dark gray objects mark where the nacelle model is employed to resolve the object. The assumed volume required for the debris accumulation in the AL-DM case is shown in yellow. The red lines demonstrate the AL, and the red triangles over the gray surface in (d) mark the AS model.

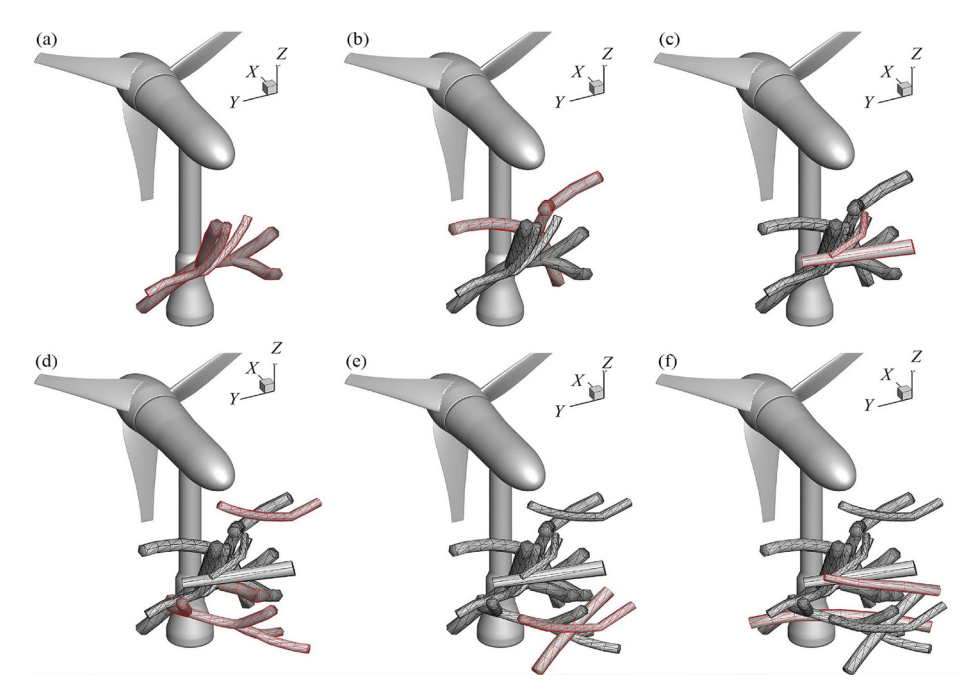


Fig. 3. The density of debris accumulation in various cases is when on the TR-DR case. Going from case 1 (a) to case 6 (f), the density of the woody debris increases (see Table 1). The red logs indicate the additional logs added to construct new denser cases.

chosen such that the maximum Courant-Friedrichs-Lewy (CFL) number is less than 1.0. Given the approaching flow velocity of $U_{\infty}=1.56$ m/s and the rotor diameter 5 m, the flow had a Reynolds number of 7.8×10^6 .

The wall model approach was employed to incorporate the hydrodynamics effect of the solid surfaces of the sidewalls, channel bed, wood debris, and turbine components on the turbulent flow. The free surface of the flow was described using a rigid-lid assumption. Neumann boundary conditions were used at the outlet cross-place of the flow. At the inlet cross-plane of the flume, we imposed a previously generated instantaneous turbulent flow, which was developed through a separately done precursor simulation [68].

The numerical simulations of the turbine resolving and actuator line model cases were carried out using 96 processors for nearly 4500 and 2500 CPU hours on a Linux cluster (AMD Epyc). In other words, our turbine-resolving simulations were approximately 80% more expensive computationally than those with actuator models. In addition, the simulations using the debris resolving method and debris model were conducted using 96 processors for about 2500 and 2300 CPU hours, respectively. Hence, the simulations with the debris model to represent the wood piles were roughly 10% less expensive computationally than the debris-resolving simulations. Lastly, based on this analysis, simulations

with the AS model were about 40% more expensive computationally than those with the AL model.

4. Results and discussion.

4.1 Hydrodynamic impacts of debris accumulations. We start by presenting the hydrodynamic impact of debris accumulations on the turbulent flow field around the MHK turbine (see Fig. 4). As seen in Fig. 4(a)–(d), for all cases of the TR, AS, and AL, vortex shedding mechanisms can be observed at the tip of the blades, around the tower, and in the woody debris. The instantaneous vortical coherent structures are visualized with the iso-surfaces of Q-criterion (= 10), colored by normalized velocity magnitude. As seen in Fig. 4(a), (b), and (d) for the debris resolving cases, the LES has captured a more detailed turbulent shedding behind the larger debris piles. As a result, in the debris-resolving case, there is a more pronounced turbulent fluctuation in the vicinity of the turbine blades and at the upper regions of the MHK. The debris model, however, seems to dampen the vortical flow structures such that they have disappeared from the lower flow depth (Fig. 4(c)).

Additionally, the turbine resolving results with the debris resolving method demonstrate the resolution of more detailed turbulent flow structures compared to the actuator model numerical results. We note that such differences in the resolution of turbulent flow structures and, consequently, their fluctuating effects are expected to impact the vari-

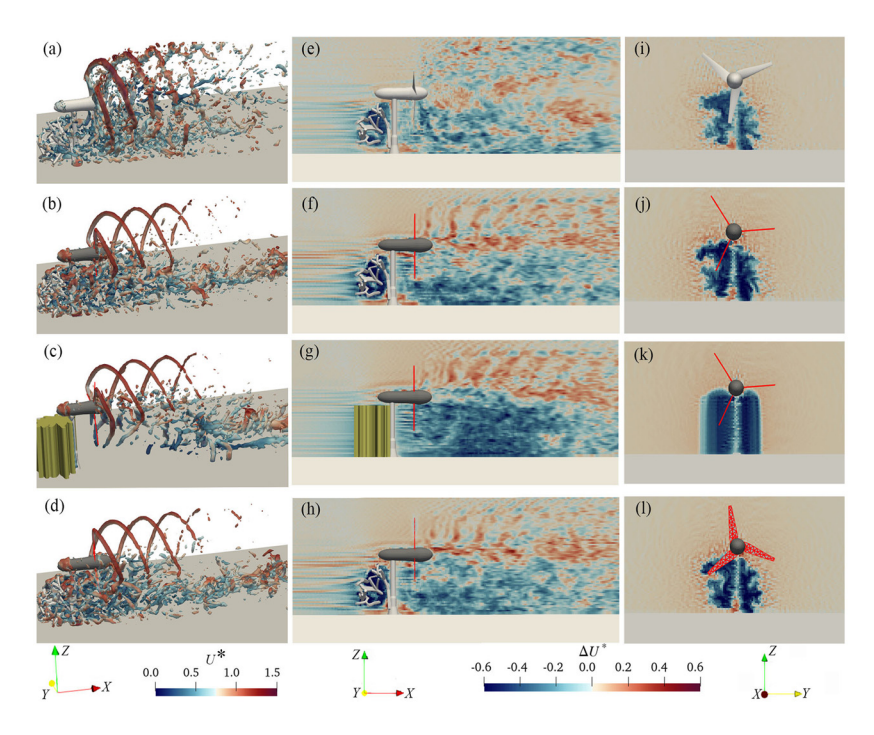


Fig. 4. LES results of different model configurations for case 6 from 3D view (a-d), side view over the centerline of the channel (e-h), and cross-section view 0.2D upstream of the turbine (i-l). In (a-d), we plot the iso-surfaces of flow structures visualized by the iso-surfaces of criterion (= 10) using TR-DR (a), AL-DR (b), AL-DM (c), and AS-DR (d) model configurations. The iso-surfaces are colored with normalized velocity magnitude, $U^* = \frac{U}{U_{\infty}}$ where U_{∞} is 1.56 m/s. The color maps in (e-l) plot the contours of instantaneous velocity magnitude differences between case 6 and case 0 (nondimensionalized by U_{∞} , $\Delta U^* = (U_{\text{case-6}} - U_{\text{Case-0}})/U_{\infty}$) with TR-DR (e,i), AL-DR (f,j), AL-DM (g,k), and AS-DR (h,l) model configurations. Notably, the velocity field of case 0 is subtracted from the velocity fields of case 6 to eliminate turbine rotation effects, thereby allowing to focus exclusively on the impact of wood logs and, thus, visualize the momentum deficit due to the debris.

ations of power productions obtained from various numerical methods. The computed power production and its variations will be discussed in the next section.

Figure 4 (b), (d), (f), (h), (i) and (j) plots the simulation results corresponding to the debris resolution for the AL and AS models, respectively. The simulation results of the AL and AS models are similar, demonstrating that the two actuator models could obtain somewhat similar results for the momentum deficit. Such similarity in the LES computations of momentum deficit using the AL and AS models for a single utility-scale wind turbine was also observed by Sotiropoulos and Khosronejad [69]. Moreover, the two actuator models obtain velocity fields with less turbulent fluctuations than the turbine-resolving case at the rotor region. As motioned, this level of turbulence fluctuations could very well play itself in power production. Finally, it is noted that the debris model could play a key role in reducing the simulations' computational cost. It is essential, however, to note that using the debris model - as opposed to the debris resolving method - has led to a significant increase in the velocity deficit at mid-depth and the lower region of the flow depth (Fig. 4(g)).

4.2 Debris impact on power production. Herein, we focus our attention on the effect of debris piles on the power production of the MHK. As discussed above, the debris-induced modulations of the MHK wake flow are also expected to play a crucial role in the variation of power production. To examine the impact of debris piles on the power generation of the MHK, we analyzed the computed results of the mean and instantaneous power generation. No matter how it is resolved, the debris accumulation over the turbine tower modifies the power outputs of the simulated MHK turbine. More importantly, it will be shown that the turbine efficiency is modulated due to debris. In particular, the reduction in efficiency is due to the flow bypassing around the debris, which diverts the flow towards the lower region of the turbine. The debris's density and frontal area augment the intensity of the flow diversion, reducing turbine efficiency. In other words, as the number of woody logs increases, the debris's frontal area increases, consequently decreas-

ing the turbine efficiency. We evaluate the turbine efficiency using the power coefficient, $C_{\rm P}$ (= $2P/\rho AU_{\infty}^3$), where P is the calculated power of the turbine) [53].

In Fig. 5, we plot the mean power coefficient (C_P) and the mean of its variation amplitude $(\overline{\Delta P})$ for different debris frontal areas that are computed using the various modeling approaches. The amplitude of the mean power variations is defined as the difference between the maximum and minimum power production. Figure 5(a) shows that the power coefficient varies between 0.16 and 0.26. For the highest debris density as opposed to the case without debris, the power coefficient reduction of the turbine resolving case is about 2%, while the actuator model computations show a nearly 38% reduction in the power coefficient. The extraction of momentum from the flow due to debris decreased the power

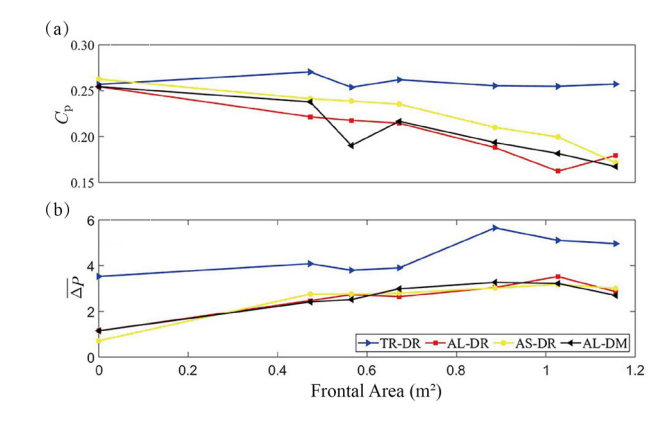


Fig. 5. Computed power coefficient (a) and mean power variation amplitude (b) for various debris densities represented by the frontal area (see Table 1) and using TR-DR, AL-DR, AL-DM, and AS-DR approaches.

coefficient of actuator model calculations. However, this trend is less pronounced for the turbine-resolving case, possibly due to the increased turbulence intensity induced by the debris.

As seen in Fig. 5(b), the mean power variation amplitude $(\overline{\Delta P})$ for all test cases is marked with an increasing trend. The turbulence fluctuations and vortex shedding intensity increase with new woody debris added to the pile. As a result, the turbine's power production in all cases contains more significant oscillations. As seen, such fluctuations in both turbulence and power production are more pronounced for the turbine-resolving case.

Furthermore, we analyze the time series of power generation to examine the impact of debris piles and numerical methods on its temporal fluctuation. In Fig. 6, we plot the time history of power production versus the number of blade revolutions. After about five revolutions, a consistent power production pattern is observed for each case, prompting a systematic analysis of up to five revolutions. In this figure, the simulation results are referred to as case 0, represented by a solid blue line, which marks the case of the MHK turbine without debris. Aside from the MHK turbine, no obstacles induce turbulent fluctuations in this case. As a result, a rapid convergence of power production at around half of the first revolution is obtained. More specifically, the leading cause of the power fluctuation in case 0 is the passage of one of the blades in the lower region of the MHK, where the persistent wake zone of the turbine tower exists. We note that the amplitude of power production fluctuations in case 0 is about 3.4 kW and 1.1 kW for the turbine resolving and actuator models, respectively.

As discussed above, the turbine-resolving and debris-resolving methods produced a consistent mean power coefficient throughout the turbine revolution, regardless of the turbulent fluctuations caused by the debris piles. This is consistent with the instantaneous power curve in Fig. 6(a), as the average power amplitude in this figure stays relatively constant during the simulations - after the first revolution. Further, the variations of momentum deficit, ΔU^* , at the lower region of the wake in Fig. 4(e) could explain the temporal instability of the local velocity and its drastic changes near the rotor blade, which, in turn, leads to different torque values and, thus, power fluctuations. We argue that this relatively constant power variation (i.e., minor changes in the power amplitude and the mean power coefficient) for the turbine-resolving and debris-resolving case could be attributed to the 3D effects of the blade geometry. We note that this method is the only one that considers the exact geometry of the turbine blades. Figure 4(a) shows that the tip vortices and the turbulent flow structures generated around the rotating blades are more dominant than those from the debris pile. Therefore, in this case, the blade-generated turbulent fluctuations seem to overwhelm the fluctuations induced by the debris pile.

On the contrary, since the actuator models lack the three-dimensionality of the blade-resolving method, they under-resolve the strength of the blade-generated turbulent flow structures. As a result, the debris-generated turbulent fluctuation plays a more dominant role in the actuator model results. As seen in Fig. 6(b) and (d), increasing the density of the debris leads to two noticeable changes: (1) a decrease in power production for successively larger debris piles and (2) a more significant variability in temporal power output. The turbulent shedding past the denser debris pile produced more significant turbulent fluctuations in the turbine's wake region, influencing the power production's temporal variation. The power range from crest to trough of the power curve tends to increase with the frontal area of debris. However, eventually, it reaches a relatively constant temporal variation as the number of revolutions increases.

The similarity of the power curve between the debris-resolving method (Fig. 6(b)) and the debris model (Fig. 6(c)) - both obtained using the actuator line model - demonstrates that the loss in momentum imparted by the debris model accurately captures the debris effect. However, the debris model behaves slightly differently than the debris-resolving method. It distributes the debris effects uniformly over the permeable volume, constraining the variations in the momentum and, consequently, the power production curve.

Additionally, in Fig. 7, we examine the frequency distribution of the power generation by carrying out power spectra density analysis. In this figure, dimensionless frequency $(f2\pi/\omega)$ is obtained from the frequency (f) and the angular velocity of the rotor (ω) . As seen, for all cases, the peak spectrum occurs at $f2\pi/\omega$ of approximately 10, corresponding to a third of one rotor revolution. This is consistent with the findings of Kang et al. [25] for laboratory-scale turbines. In Fig. 7(a), however, the turbine- and debris-resolving methods induced strong signals at high frequencies $(f2\pi/\omega>10)$. We argue that these signals are correlated with the high power fluctuations due to the debris cluster observed in Fig. 6(a). On the other hand, employing the turbine actuator and/or debris models entailed a signal cut-off at frequencies $f2\pi/\omega>35$. Nonetheless, at frequencies smaller than 35, actuator models incorporated with debris-resolving and debris model demonstrated in Fig. 7(b), (c), and (d) predicted low-frequency region accurately.

5. Conclusion. Freely floating debris encountering man-made structures could collect over the structures and impact the efficiency of the MHK turbines. Experimental or field studies of such impacts often entail logistical difficulties or Reynolds number limitations. We studied the impact of debris accumulations on the efficiency of a utility-scale

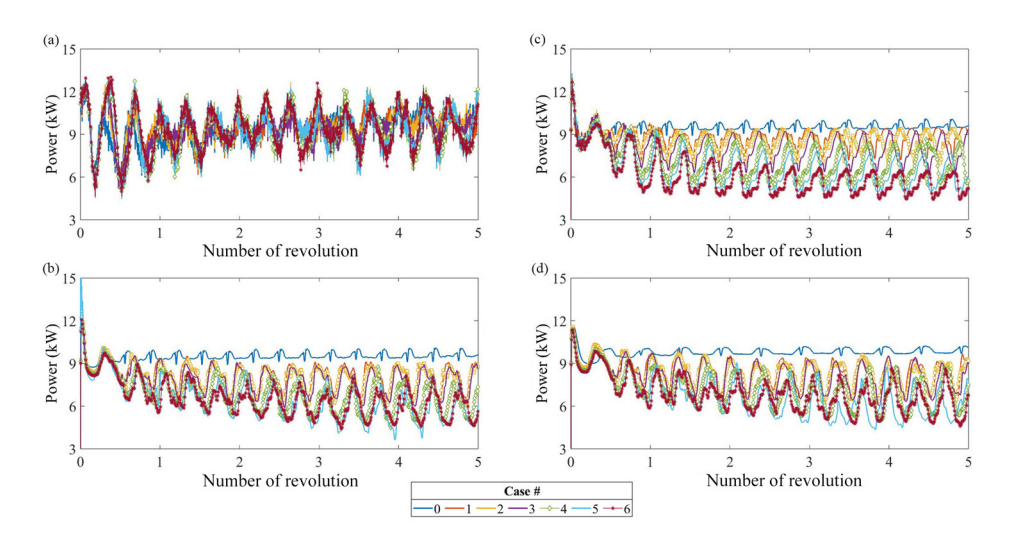


Fig. 6. Instantaneous power production in terms of turbine revolution for cases 0 to 6. The power curves are obtained by (a) TR-DR, (b) AL-DR, (c) AL-DM, and (d) AS-DR.

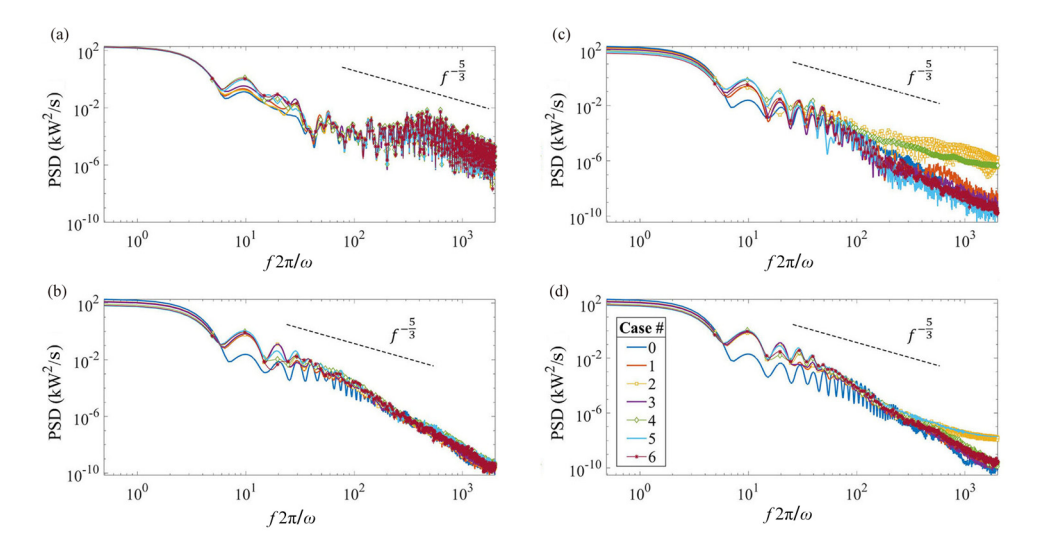


Fig. 7. Power spectral density analysis of the turbine power production in terms of $f2\pi/\omega$ for cases 0 to 6. f denotes the frequency, and ω is the rotor's angular velocity. The spectral analysis is obtained by (a) TR-DR, (b) AL-DR, (c) AL-DM, and (d) AS-DR method.

MHK turbine using the LES and various debris and blade-resolving techniques. Namely, we employed the following methods to model the blade and debris: (a) TR-DR, (b) AL-DR, (c) AL-DM, and (d) AS-DR. Moreover, a series of randomly positioned debris accumulations were systematically investigated. Although this study assumes only a limited number of possible debris accumulations, the findings of this study could (1) provide an improved understanding of debris impact on MHK turbines' efficiency, (2) mark the critical effect of debris accumulation on MHK performance in the field, and (3) propose methods of investigating the effect of debris accumulations on the efficiency of MHK turbines.

The impact of debris accumulation on the mean power coefficient and instantaneous power fluctuation appears to be correlated with the amount of upstream blockage of the flow, as reflected by the projected frontal area of debris. This is mainly due to the loss of momentum in the flow past the debris and an increase in turbulent fluctuations. In other words, the denser the debris accumulation, the greater the wake deficit at the lower depths, while the less pronounced turbulent fluctuation in the mid-depth region of the flow.

Additionally, it was found that the geometry-resolving methods are advantageous in describing the near-field characteristics, enabling a more detailed representation of the flow field near the blade. Given the CPU times of the debris-resolving and debris models, additional computational costs due to employing the debris-resolving method may be conceded for specific studies since the geometry-resolving method captures the flow-debris-MHK interactions better. Nonetheless, the debris model may benefit if an increase in the complexity of debris buildups or incorporating the debris accumulation with larger scale works are considered. The turbine-resolving approach can better capture the fluctuating nature of the turbulent flow field and, consequently, the power production. As a result, the power production of the turbine-resolving method contains a great deal of fluctuation with greater power amplitude than that of the actuator models. Since the geometry-resolving method refers to the reference for reduced-order methods, representing the blade with simplified models reduces the accuracy of the power production, which is to be acknowledged. However, actuator models provide practical tools with relatively low computational costs to simulate utility-scale MHK turbines in natural terrains. Moreover, the proposed debris model could generate reliable realizations of 3D debris accumulations. This method is especially useful for eliminating the need to know the precise positioning of the debris logs as it distributes their associated drag force over a given debris volume within the computational domain.

This study encompasses the impacts of debris accumulation on the MHK turbine by utilizing various turbine and debris models with different debris densities. For that, in total, we numerically studied 28 cases. After conducting a grid sensitivity analysis, we selected a grid resolution that allowed us to complete these numerical simulations, given the limited computing power at our disposal. Yet, it should be noted that increasing the grid resolution would allow the capture of a wide range of turbulent eddies and, thus, improve the power production computations, especially using the turbine geometry-resolving method. Additionally, for future studies, we will seek experimental data for debris accumulation on the turbine tower with non-uniform characteristics at realistic Reynolds numbers to validate further the model's wake flow and power production computations.

Further studies are required to investigate the impact of debris accumulation on the sediment transport around the base of the turbine tower. More importantly, in future research, we plan to validate the model's simulation results for the wake flow field and power production against experimental data of turbine and debris accumulation.

Data availability statement

The code for the numerical model, including the debris model and actuator models (10.5281/zenodo.10521565), simulation results for the flow field (10.5281/zenodo.10521509), and power production of the test cases (10.5281/zenodo.10521545) are made available in the online repository of Zenodo.

Declaration of competing interest

The authors declare that they have no known competing financial interests or personal relationships that could have appeared to influence the work reported in this paper.

CRediT authorship contribution statement

Mustafa Meriç Aksen: Investigation, Software, Validation, Writing – original draft, Writing – review & editing. Kevin Flora: Conceptualization, Data curation, Formal analysis, Investigation, Methodology, Software, Validation, Writing – review & editing. Hossein Seyedzadeh: Formal analysis, Investigation, Writing – original draft. Mehrshad Gholami Anjiraki: Investigation, Validation, Writing – original draft. Ali Khosronejad: Conceptualization, Data curation, Formal analysis, Funding acquisition, Methodology, Project administration, Resources, Soft-

ware, Supervision, Visualization, Writing – original draft, Writing – review & editing.

Acknowledgements

This work was supported by the United States Department of Energy's Office of Energy Efficiency and Renewable Energy (EERE) under the Water Power Technologies Office (WPTO) (Grant No. DE-EE0009450). Partial support was also provided by the National Science Foundation (Grant No. 2233986). The views expressed herein do not necessarily represent the view of the U.S. Department of Energy or the United States Government. The Civil Engineering Department, Stony Brook Research Computing and Cyber Infrastructure, and the Institute for Advanced Computational Science at Stony Brook University provided the computational resources.

Appendix A. Validation study

The LES results of the model with the turbine-resolving and actuator line parametrizations were validated using experimental data reported in [67]. The validation case includes a downstream-facing horizontal-axis turbine (i.e., Gen4 kinetic hydropower system) with a diameter of D=0.16 m and a constant tip speed ratio of $\lambda=5.1$, installed in a flume with a bulk flow velocity of $U_{\infty}=0.19$ m/s (Fig. A1). With the given bulk velocity and rotor diameter, the Reynolds number is 3.51×10^4 .

We replicated the experiment using a nonuniform grid system for the computational domain of the flume. More specifically, the red rectangles in Fig. A1 represent the regions of the computational domain where a uniform grid system with a resolution of 0.0029 m in all directions was employed. Outside the region illustrated with the red lines, the vertical resolution remained the same while the grid system was stretched horizontally, reaching maximum spatial resolution of 0.0086 m and 0.012 m in the streamwise and spanwise directions, respectively (see Table A1). A time step of 0.0025 s was used to ensure that the CFL

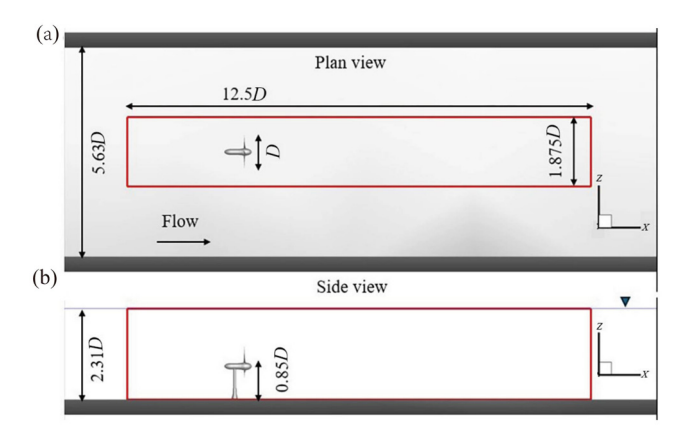


Fig. A1. Schematic of the simulated experimental MHK turbine in the flume from the top (a) and side view (b). Dimensions are normalized with the rotor diameter D (= 0.16 m). The turbine's hub height is 0.85D. Red lines show the volume of the flume where uniform grid nodes are applied. In the remaining part of the channel, the grid spacings were stretched in the streamwise and spanwise directions.

number was less than 1.0. Additionally, we introduced an instantaneous turbulent flow at the inlet cross-plane of the flume. The turbulent inflow was generated through an independent precursor simulation. The wall model (presented in Section 2.3) was used to reconstruct the velocity field near the solid surfaces. Once the instantaneous data reached convergence, we time-averaged the flow field results for mean velocity and Reynolds stresses to compare with the measurements of Lee et al. [67].

In Fig. A2, we compare the measured and computed contour plot of the mean axial velocity along the streamwise direction. As seen, the turbine-resolving and actuator line models exhibit a relatively good qualitative agreement with the measured results. However, the size of

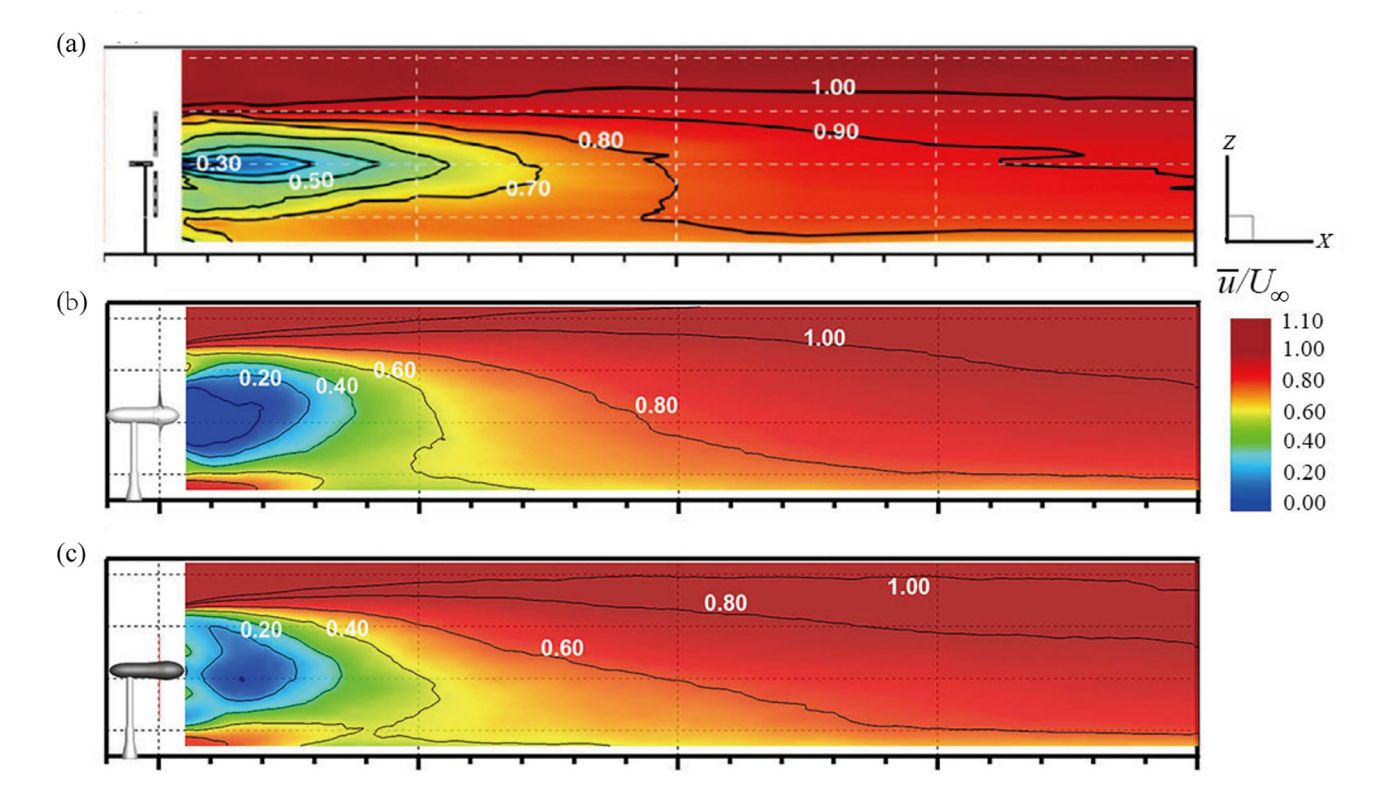
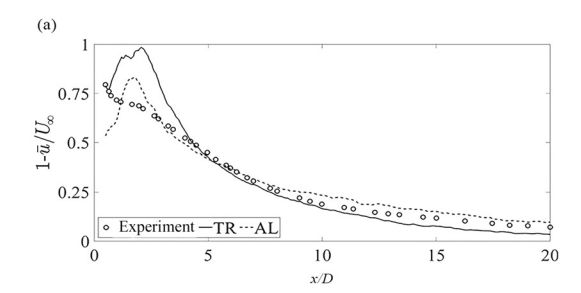


Fig. A2. Contour plots of time-averaged normalized mean velocity fields obtained from (a) the experiment of [67], (b) computed using the turbine-resolving method, and (c) the actuator-line model. The mean velocity is normalized with the incoming velocity at the hub height. Side view was taken over the centerline of the channel. The mean velocity fields are plotted from 0.5*D* to 20*D* downstream of the nacelle.



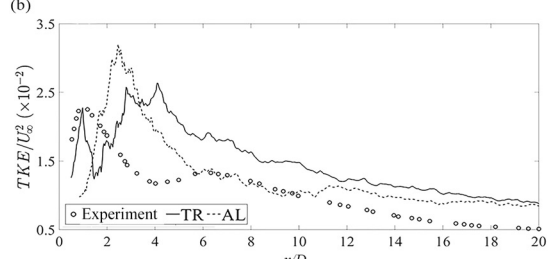


Fig. A3. Longitudinal profiles of (a) the normalized mean axial velocity and (b) turbulence kinetic energy (TKE), starting from 0.5D downstream of the rotor to 20D in the streamwise direction at hub height (= 0.85D). The parameters are normalized by the bulk velocity ($U_{\infty} = 0.19$ m/s) at the hub height. The hollow circles, bold lines, and dashed lines represent the measured, turbine-resolving method, and actuator-line model computations, respectively.

Table A1

The computational details of the numerical simulation for the model validation. $\Delta x_{\rm b}, \ \Delta y_{\rm b}, \ {\rm and} \ \Delta z_{\rm b}$ are dimensional uniform grid spacings near the blade in streamwise, spanwise, and vertical directions. $\Delta x_{\rm max}, \ \Delta y_{\rm max}, \ {\rm and} \ \Delta z_{\rm max}$ are dimensional maximum grid spacings outside the refined region of the computational domain. Δz^+ is the grid spacing in wall units near the blade. Δt^* is the non-dimensional time step, defined as $\Delta t^* = \Delta t(U_{\infty}/D)$, where Δt is the dimensional time step.

Variable	Grid
N_x, N_y, N_z	221 × 129 × 2421
$\Delta x_{\rm b}, \Delta y_{\rm b}, \Delta z_{\rm b}$ (m)	0.0029
Δx_{max} , Δy_{max} , Δz_{max} (m)	0.0086, 0.012, 0.0029
Δz^+	225
Δt^*	0.0025

the wake deficit region was overestimated, while the minimum wake velocity was underestimated. In Fig. A3, the LES computations of the model were quantitatively validated with the mean velocity and turbulence kinetic energy along streamwise profiles. The computed velocity and TKE are overestimated in the near field, while the results reach a reasonable agreement in the far wake.

Appendix B. Grid sensitivity analysis

We carried out a grid independence analysis to investigate the effect of grid resolution on the model computations for case 6 of the study. We employ three successively refined spatial resolutions, resulting in 9 to 40 million computational grid nodes. The three grid systems, from finest to coarsest grid, are denoted as grid I, grid II, and grid III, respectively (Table B1). As seen in Fig. B1, the instantaneous power production of

Table B1

The computational details of the numerical simulations for different grid systems. N_x, N_y , and N_z are the number of computational grid nodes in the streamwise, spanwise, and vertical directions. Δt^* is the non-dimensional time step, defined as $\Delta t(U_\infty/D)$, where Δt is the dimensional time step. Δz^+ is minimum grid spacing scaled in inner wall units and defined as $u_*\Delta z/v$, where u_* is the shear velocity computed by the wall model.

Variable	Grid I	Grid II	Grid III
Number of grid nodes	40×10^{6}	19×10^{6}	9×10^{6}
N_x, N_y, N_z	$349 \times 109 \times 1025$	$881 \times 253 \times 81$	$209 \times 68 \times 585$
$\Delta x, \Delta y, \Delta z$ (m)	0.015	0.02	0.025
Δt^*	0.001	0.001	0.001
Δz^+	800	1000	1400

the actuator line and debris resolving model was compared to find the suitable grid resolution with the lowest computational cost. As seen in this table, the near wall grid resolution is of $\Delta z^+ \geq 800$. We note that the performance of the present wall model at this near-wall grid resolution was validated against a series of experimental and field-measured data [45,49,59]. In particular, [59] validated the wall model's performance against field data of a riverine flow and investigated the propagation of uncertainty in the river flow computations of the LES model due to the variations in the parameters of the wall model.

Furthermore, the instantaneous power curve plot is enlarged at the trough of the eighth cycle in the third revolution. It is noticed that while the instantaneous power production varies considerably from grid III (coarsest resolution) to grid II, the variation of instantaneous power production from grid II to grid I (finest) is negligibly small. More specifically, while the computed average power, \overline{P} (= $\sum_{i=0}^{i=N} P_i/N$, where N is the number of time steps) with grid I and II varies around 1%, the nu-

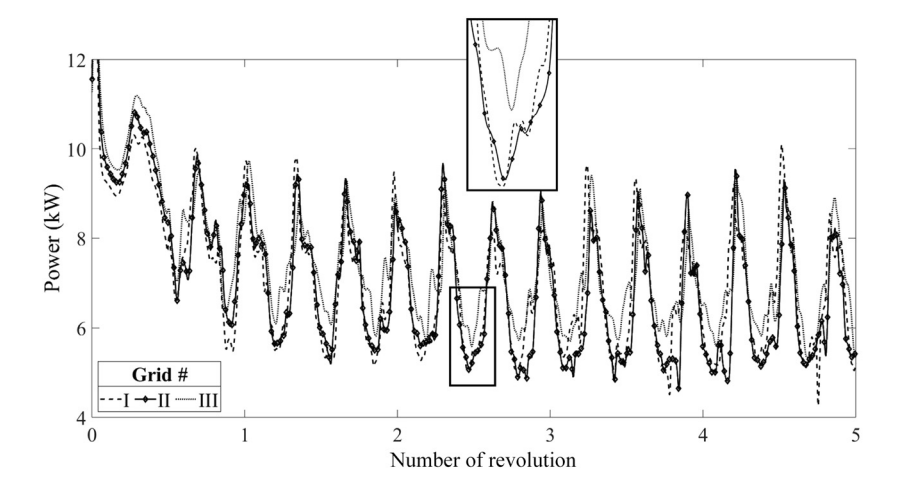


Fig. B1. Instantaneous power production in terms of turbine revolution for case 6 of actuator line and debris-resolving method. Dash, solid with diamond marker, and dotted lines show the computed results of grid I (fine), II, and III (coarse), respectively.

merical errors due to the grid resolution difference between grids II and III is nearly 6%. Therefore, grid II was considered for the simulations of this study.

References

- [1] R. Roche, K. Walker-Springett, P. Robins, J. Jones, G. Veneruso, T. Whitton, M. Piano, S. Ward, C. Duce, J. Waggitt, G. Walker-Springett, S. Neill, M. Lewis, J. King, Research priorities for assessing potential impacts of emerging marine renewable energy technologies: insights from developments in wales (UK), Renew. Energy 99 (2016) 1327–1341, doi:10.1016/j.renene.2016.08.035. https://www.sciencedirect.com/science/article/pii/S0960148116307364
- [2] M.I. Yüce, A. Muratouglu, Hydrokinetic energy conversion systems: a technology status review, Renew. Sustain. Energy Rev. 43 (2015) 72–82, doi:10.1016/j.rser.2014. 10.037. https://www.sciencedirect.com/science/article/pii/S1364032114008624
- [3] L. Schmocker, V. Weitbrecht, Driftwood: risk analysis and engineering measures,
 J. Hydraul. Eng. 139 (7) (2013) 683–695, doi:10.1061/(ASCE)HY.1943-7900.
 0000728.
- [4] I. Schalko, L. Schmocker, V. Weitbrecht, R.M. Boes, Backwater rise due to large wood accumulations, J. Hydraul. Eng. 144 (9) (2018) 04018056, doi:10.1061/(ASCE)HY. 1943-7900.0001501.
- [5] J.P. Matthews, L. Ostrovsky, Y. Yoshikawa, S. Komori, H. Tamura, Dynamics and early post-tsunami evolution of floating marine debris near Fukushima Daiichi, Nat. Geosci. 10 (8) (2017) 598–603, doi:10.1038/ngeo2975.
- [6] A. Hasanpour, D. Istrati, I. Buckle, Coupled SPH-FEM modeling of tsunami-borne large debris flow and impact on coastal structures, J. Mar. Sci. Eng. 9 (10) (2021), doi:10.3390/jmse9101068. https://www.mdpi.com/2077-1312/9/10/1068
- [7] L. Schmocker, W.H. Hager, Probability of drift blockage at bridge decks, J. Hydraul. Eng. 137 (4) (2011) 470–479, doi:10.1061/(ASCE)HY.1943-7900.0000319.
- [8] F.F.M. Chang, H.W. Shen, Debris problems in the river environment, 1979. https://api.semanticscholar.org/CorpusID:126621304
- [9] P. Lagasse, J. Schall, E. Richardson, Stream stability at highway structures, 3rd ed. (2001). https://www.rosap.ntl.bts.gov/view/dot/57155.
- [10] P.F. Lagasse, P.E. Clopper, L.W. Zevenbergen, W.J. Spitz, L.G. Girard, Effects of Debris on Bridge Pier Scour, The National Academies Press, Washington, DC, 2010, doi:10.17226/22955
- [11] D. Panici, P. Kripakaran, Characterizing the importance of porosity of large woody debris accumulations at single bridge piers on localized scour, Water Resour. Res. 59 (9) (2023), doi:10.1029/2022WR033531. e2022WR033531
- [12] J. Jeon, Y. Kim, D. Kim, S. Kang, Flume experiments for flow around debris accumulation at a bridge, KSCE J. Civ. Eng. (2024) 1–13, doi:10.1007/s12205-024-1442-4.
- [13] C. Hill, M. Musa, L.P. Chamorro, C. Ellis, M. Guala, Local scour around a model hydrokinetic turbine in an erodible channel, J. Hydraul. Eng. 140 (8) (2014) 04014037, doi:10.1061/(ASCE)HY.1943-7900.0000900.
- [14] C. Hill, M. Musa, M. Guala, Interaction between instream axial flow hydrokinetic turbines and uni-directional flow bedforms, Renew. Energy 86 (2016) 409–421, doi:10.1016/j.renene.2015.08.019. https://www.sciencedirect.com/science/article/pii/S0960148115302196
- [15] C. Hill, J. Kozarek, F. Sotiropoulos, M. Guala, Hydrodynamics and sediment transport in a meandering channel with a model axial-flow hydrokinetic turbine, Water Resour. Res. 52 (2) (2016) 860–879, doi:10.1002/2015WR017949.
- [16] M. Musa, C. Hill, F. Sotiropoulos, M. Guala, Performance and resilience of hydrokinetic turbine arrays under large migrating fluvial bedforms, Nat. Energy 3 (10) (2018) 839–846, doi:10.1038/s41560-018-0218-9.
- [17] X. Yang, A. Khosronejad, F. Sotiropoulos, Large-eddy simulation of a hydrokinetic turbine mounted on an erodible bed, Renew. Energy 113 (2017), doi:10.1016/j. renene.2017.07.007.
- [18] R. Ramírez-Mendoza, L. Amoudry, P. Thorne, R. Cooke, S. McLelland, L. Jordan, S. Simmons, D. Parsons, L. Murdoch, Laboratory study on the effects of hydro kinetic turbines on hydrodynamics and sediment dynamics, Renew. Energy 129 (2018) 271–284, doi:10.1016/j.renene.2018.05.094. https://www.sciencedirect.com/science/article/pii/S0960148118306190
- [19] M. Musa, M. Heisel, M. Guala, Predictive model for local scour downstream of hydrokinetic turbines in erodible channels, Phys. Rev. Fluids 3 (2018) 024606, doi:10.1103/PhysRevFluids.3.024606.
- [20] T. Javaherchi, A. Aliseda, A.T. Javaherchi Mozafari, The transport of suspended sediment in the wake of a marine hydrokinetic turbine: simulations via a validated discrete random walk (DRW) model, Ocean Eng. 129 (2016), doi:10.1016/j.oceaneng. 2016.10.039.
- [21] X. Lin, J. Zhang, R. Wang, J. Zhang, W. Liu, Y. Zhang, Scour around a mono-pile foun-dation of a horizontal axis tidal stream turbine under steady current, Ocean Eng. 192 (2019) 106571, doi:10.1016/j.oceaneng.2019.106571. https://www.sciencedirect.com/science/article/pii/S0029801818320596
- [22] E. Jump, A. Macleod, T. Wills, Review of tidal turbine wake modelling methods: state of the art, Int. Mar. Energy J. 3 (2020) 91-100, doi:10.36688/imej.3.91-100. https://www.marineenergyjournal.org/imej/article/view/57
- [23] S. Chawdhary, D. Angelidis, J. Colby, D. Corren, L. Shen, F. Sotiropoulos, Multiresolution large-eddy simulation of an array of hydrokinetic turbines in a field-scale river: the roosevelt island tidal energy project in New York City, Water Resour. Res. 54 (12) (2018) 10,188–10,204, doi:10.1029/2018WR023345. https://www.agupubs.onlinelibrary.wiley.com/doi/abs/10.1029/2018WR023345. https://agupubs.onlinelibrary.wiley.com/doi/pdf/10.1029/2018WR023345
- [24] P.K. Stansby, P. Ouro, Modelling marine turbine arrays in tidal flows, J. Hydraul. Res. 60 (2) (2022) 187–204, doi:10.1080/00221686.2021.2022032.

- [25] S. Kang, X. Yang, F. Sotiropoulos, On the onset of wake meandering for an axial flow turbine in a turbulent open channel flow, J. Fluid Mech. 744 (2014), doi:10.1017/ ifm.2014.82.
- [26] S. Kang, Y. Kim, J. Lee, A. Khosronejad, X. Yang, Wake interactions of two horizontal axis tidal turbines in tandem, Ocean Eng. 254 (2022) 111331, doi:10.1016/j.oceaneng.2022.111331. https://www.sciencedirect.com/ science/article/pii/S0029801822007223
- [27] S. Chawdhary, C. Hill, X. Yang, M. Guala, D. Corren, J. Colby, F. Sotiropoulos, Wake characteristics of a TriFrame of axial-flow hydrokinetic turbines, Renew. Energy 109 (2017) 332–345, doi:10.1016/j.renene.2017.03.029. https://www.sciencedirect.com/science/article/pii/S0960148117302100
- [28] X. Yang, F. Sotiropoulos, R.J. Conzemius, J.N. Wachtler, M.B. Strong, Large-eddy simulation of turbulent flow past wind turbines/farms: the virtual wind simulator (VWIS), Wind Energy 18 (12) (2015) 2025–2045, doi:10.1002/we.1802. https://www.onlinelibrary.wiley.com/doi/pdf/10.1002/we.1802
- [29] Z. Wu, L. Guo, Accuracy improvement of immersed boundary-lattice Boltzmann and finite element method by iterative velocity correction, Phys. Fluids 34 (10) (2022) 103102, doi:10.1063/5.0110813. https://www.pubs.aip.org/aip/pof/article-pdf/ doi/10.1063/5.0110813/16573258/103102_1_online.pdf
- [30] A. Posa, R. Broglia, Analysis of the momentum recovery in the wake of aligned axial-flow hydrokinetic turbines, Phys. Fluids 34 (10) (2022) 105130, doi:10.1063/ 5.0117882.
- [31] A. Posa, R. Broglia, E. Balaras, Recovery in the wake of in-line axial-flow rotors, Phys. Fluids 34 (4) (2022) 045104, doi:10.1063/5.0085587.
- [32] A. Posa, R. Broglia, Momentum recovery downstream of an axial-flow hydrokinetic turbine, Renew. Energy 170 (2021) 1275–1291, doi:10.1016/j.renene.2021.02.061. https://www.sciencedirect.com/science/article/pii/S0960148121002299
- [33] X. Yang, F. Sotiropoulos, A new class of actuator surface models for wind turbines, Wind Energy 21 (5) (2018) 285–302, doi:10.1002/we.2162. https://www.onlinelibrary.wiley.com/doi/abs/10.1002/we.2162
- [34] J.N. Sorensen, W.Z. Shen, Numerical modeling of wind turbine wakes, J. Fluids Eng. 124 (2) (2002) 393–399, doi:10.1115/1.1471361.
- [35] M. Hansen, Aerodynamics of Wind Turbines, Routledge, 2015.
- [36] R. Mikkelsen, J.N. Sørensen, S. Øye, N. Troldborg, Analysis of power enhancement for a row of wind turbines using the actuator line technique, J. Phys. Conf. Ser. 75 (1) (2007) 012044, doi:10.1088/1742-6596/75/1/012044.
- [37] W.Z. Shen, V.A.K. Zakkam, J.N. Sørensen, K. Appa, Analysis of counter-rotating wind turbines, J. Phys. Conf. Ser. 75 (1) (2007) 012003, doi:10.1088/1742-6596/75/1/ 012003
- [38] N. Troldborg, J.N. Sorensen, R. Mikkelsen, Numerical simulations of wake characteristics of a wind turbine in uniform inflow, Wind Energy 13 (1) (2010) 86–99, doi:10. 1002/we.345. https://www.onlinelibrary.wiley.com/doi/pdf/10.1002/we.345
- [39] P. Ouro, M. Harrold, T. Stoesser, P. Bromley, Hydrodynamic loadings on a horizontal axis tidal turbine prototype, J. Fluids Struct. 71 (2017) 78–95, doi:10. 1016/j.jfluidstructs.2017.03.009. https://www.sciencedirect.com/science/article/pii/S0889974616305679
- [40] P. Ouro, L. Ramírez, M. Harrold, Analysis of array spacing on tidal stream turbine farm performance using large-eddy simulation, J. Fluids Struct. 91 (2019) 102732, doi:10.1016/j.jfluidstructs.2019.102732. https://www.sciencedirect.com/ science/article/pii/S0889974619301161
- [41] C. Liu, C. Hu, An actuator line immersed boundary method for simulation of multiple tidal turbines, Renew. Energy 136 (2019) 473–490, doi:10.1016/j.renene.2019. 01.019. https://www.sciencedirect.com/science/article/pii/S0960148119300199
- [42] Z. Gao, T. Wang, S. Ke, D. Li, Recent improvements of actuator line-large-eddy simulation method for wind turbine wakes, Appl. Math. Mech. 42 (2021), doi:10.1007/ s10483.001-2717-8
- [43] Z. Li, X. Yang, Evaluation of actuator disk model relative to actuator surface model for predicting utility-scale wind turbine wakes, Energies 13 (14) (2020), doi:10. 3390/en13143574.
- [44] Z. Gao, Y. Li, T. Wang, W. Shen, X. Zheng, S. Pröbsting, D. Li, R. Li, Modelling the nacelle wake of a horizontal-axis wind turbine under different yaw conditions, Renew. Energy 172 (2021) 263–275, doi:10.1016/j.renene.2021.02.140.
- [45] K. Flora, A. Khosronejad, On the impact of bed-bathymetry resolution and bank vegetation on the flood flow field of the American River, California: insights gained using data-driven large-eddy simulation, J. Irrig. Drain. Eng. 147 (9) (2021) 04021036, doi:10.1061/(ASCE)JR.1943-4774.0001593.
- [46] Z. Liu, Z. Diao, T. Ishihara, Study of the flow fields over simplified topographies with different roughness conditions using large eddy simulations, Renew. Energy 136 (2019) 968–992, doi:10.1016/j.renene.2019.01.032.
- [47] E. Ng, C. Yuan, L. Chen, C. Ren, J.C. Fung, Improving the wind environment in high-density cities by understanding urban morphology and surface roughness: a study in Hong Kong, Landscape Urban Plann. 101 (1) (2011) 59–74, doi:10.1016/j. landurbplan.2011.01.004.
- [48] R.H. Shaw, U. Schumann, Large-eddy simulation of turbulent flow above and within a forest, Boundary-Layer Meteorol. 61 (1) (1992) 47–64, doi:10.1007/BF02033994.
- [49] K. Flora, C. Santoni, A. Khosronejad, Numerical study on the effect of bank vegetation on the hydrodynamics of the american river under flood conditions, J. Hydraul. Eng. 147 (9) (2021) 05021006, doi:10.1061/(ASCE)HY.1943-7900.0001912.
- [50] H. Abedi, S. Sarkar, H. Johansson, Numerical modelling of neutral atmospheric boundary layer flow through heterogeneous forest canopies in complex terrain (a case study of a swedish wind farm), Renew. Energy 180 (2021) 806–828, doi:10.1016/j.renene.2021.08.036.
- [51] H. Abedi, Assessment of flow characteristics over complex terrain covered by the heterogeneous forest at slightly varying mean flow directions, Renew. Energy 202 (C) (2023) 537–553. doi:10.1016/j.renene.2022.11.
- [52] A. Khosronejad, F. Sotiropoulos, Numerical simulation of sand waves in a turbu-

- lent open channel flow, J. Fluid Mech. 753 (2014) 150–216, doi:10.1017/jfm.2014.
- [53] S. Kang, I. Borazjani, J.A. Colby, F. Sotiropoulos, Numerical simulation of 3D flow past a real-life marine hydrokinetic turbine, Adv. Water Resour. 39 (2012) 33–43, doi:10.1016/j.advwatres.2011.12.012. https://www.sciencedirect. com/science/article/pii/S0309170811002533
- [54] L. Ge, F. Sotiropoulos, A numerical method for solving the 3D unsteady incompressible Navier-Stokes equations in curvilinear domains with complex immersed boundaries, J. Comput. Phys. 225 (2) (2007) 1782–1809, doi:10.1016/j.jcp.2007.02.017. https://www.sciencedirect.com/science/article/pii/S0021999107000873
- [55] A. Khosronejad, J.L. Kozarek, F. Sotiropoulos, Simulation-based approach for stream restoration structure design: model development and validation, J. Hydraul. Eng. 140 (9) (2014) 04014042, doi:10.1061/(ASCE)HY.1943-7900.0000904.
- [56] A. Khosronejad, S. Kang, I. Borazjani, F. Sotiropoulos, Curvilinear immersed boundary method for simulating coupled flow and bed morphodynamic interactions due to sediment transport phenomena, Adv. Water Resour. 34 (7) (2011) 829–843, doi:10.1016/j.advwatres.2011.02.017.
- [57] I. Borazjani, L. Ge, F. Sotiropoulos, Curvilinear immersed boundary method for simulating fluid structure interaction with complex 3D rigid bodies, J. Comput. Phys. 227 (16) (2008) 7587–7620, doi:10.1016/j.jcp.2008.04.028.
- [58] A. Khosronejad, A.B. Limaye, Z. Zhang, S. Kang, X. Yang, F. Sotiropoulos, On the morphodynamics of a wide class of large-scale meandering rivers: insights gained by coupling LES with sediment-dynamics, J. Adv. Model. Earth Syst. 15 (3) (2023), doi:10.1029/2022MS003257. e2022MS003257
- [59] K. Flora, A. Khosronejad, Uncertainty quantification of large-eddy simulation results of riverine flows: a field and numerical study, Environ. Fluid Mech. 22 (2022) 1135– 1159, doi:10.1007/s10652-022-09882-1.
- [60] S. Yokojima, Y. Kawahara, T. Yamamoto, Effect of vegetation configuration on turbulent flows in a rectangular open channel, in: Proc. Of 35th IAHR World Congress, Chengdu, China, 2013.

- [61] T. Morinaga, N. Tanaka, J. Yagisawa, S. Karunaratne, W. Weerakoon, Estimation of drag coefficient of trees considering the tree bending or overturning situations, 2012. https://www.api.semanticscholar.org/CorpusID:55137242
- [62] V.S. Fred Sonnenwald, I. Guymer, Estimating drag coefficient for arrays of rigid cylinders representing emergent vegetation, J. Hydraul. Res. 57 (4) (2019) 591–597, doi:10.1080/00221686.2018.1494050.
- [63] C. Santoni, A. Khosronejad, P. Seiler, F. Sotiropoulos, Toward control co-design of utility-scale wind turbines: collective vs. individual blade pitch control, Energy Rep. 9 (2023) 793–806, doi:10.1016/j.egyr.2022.12.041.
- [64] C. Santoni, A. Khosronejad, X. Yang, P. Seiler, F. Sotiropoulos, Coupling turbulent flow with blade aeroelastics and control modules in large-eddy simulation of utilityscale wind turbines, Phys. Fluids 35 (1) (2023) 015140. doi:10.1063/5.0135518.
- [65] W.Z. Shen, R. Mikkelsen, J.N. Sørensen, C. Bak, Tip loss corrections for wind turbine computations, Wind Energy 8 (4) (2005) 457–475, doi:10.1002/we.153.
- [66] X. Yang, X. Zhang, Z. Li, G.-W. He, A smoothing technique for discrete delta functions with application to immersed boundary method in moving boundary simulations, J. Comput. Phys. 228 (20) (2009) 7821–7836, doi:10.1016/j.jcp.2009.07.023.
- [67] J. Lee, Y. Kim, A. Khosronejad, S. Kang, Experimental study of the wake characteristics of an axial flow hydrokinetic turbine at different tip speed ratios, Ocean Eng. 196 (2020) 106777, doi:10.1016/j.oceaneng.2019.106777.
- [68] A. Khosronejad, K. Flora, S. Kang, Effect of inlet turbulent boundary conditions on scour predictions of coupled LES and morphodynamics in a field-scale river: bankfull flow conditions, J. Hydraul. Eng. 146 (4) (2020) 04020020, doi:10.1061/(ASCE)HY. 1943-7900.0001719.
- [69] C. Santoni, F. Sotiropoulos, A. Khosronejad, A comparative analysis of actuator-based turbine structure parametrizations for high-fidelity modeling of utility-scale wind turbines under neutral atmospheric conditions, Energies 17 (3) (2024), doi:10. 3390/en17030753. https://www.mdpi.com/1996-1073/17/3/753